PAPER • OPEN ACCESS

The generation mechanism and identification of spatially non-continuous error in integral multi-station measurement systems

To cite this article: Rui Deng *et al* 2023 *Meas. Sci. Technol.* **34** 085007

View the article online for updates and enhancements.

The generation mechanism and identification of spatially non-continuous error in integral multi-station measurement systems

Rui Deng, Shendong Shi[*], **Linghui Yang, Jiarui Lin and Jigui Zhu**

State Key Laboratory of Precision Measuring Technology and Instruments, Tianjin University, Tianjin 300072, People's Republic of China

E-mail: ssd2168@tju.edu.cn

Abstract

The integral multi-station measurement system represented by indoor GPS, workshop Measuring and Positioning System or a multi-camera system, realizes high-precision 3D measurement in large-scale space by constructing a global measurement field within a unified temporal-spatial reference. In advanced equipment manufacturing sites such as robot machining, large component (the fuselage or wing of airplanes) assembly and monitoring, the integral multi-station measurement system overcomes the drawbacks of the single-station measurement system such as laser tracker that can hardly balance the measurement range and accuracy. However, with the improvement of automation and intelligence degree in equipment manufacturing, the requirements on accuracy and robustness has become more and more strict, which is a huge challenge to existing measuring technologies. Limited by the measurement principle of multi-observation intersection, the change of geometry constraint in the integral multi-station measurement field will lead to spatially non-continuous error, degrading the performance of the integral multi-station measurement system. In this paper we first analyze the mechanisms and characteristics of spatially non-continuous error at the geometry constraint level. Basing on the error propagation model, a criterion for evaluating the significance of non-continuous error is then proposed for error identification. Finally, simulations and experiments are carried out, and this proposed criterion is verified to be effective.

Keywords: integral multi-station measurement system, spatially non-continuous error, error propagation, significance criterion

(Some figures may appear in colour only in the online journal)

---

[*] Author to whom any correspondence should be addressed.

1. Introduction

In recent years, with the development of manufacturing technology, digital collaborative manufacturing has become one of the key technologies for enhancing the manufacturing quality and efficiency of large-scale equipment such as airplanes and ships [1–4]. It proposes new challenges to existing measurement systems in the aspects of large-scale coverage, high accuracy and continuous measurement capacity in complicated environment [5].

Restricted by the measurement range, the single-station measurement systems such as laser tracker (LT) needs to be moved to several stations during the measurement progress for better space coverage, as shown in the yellow zone in figure 1. The local coordinate frames at different stations are connected in a series mode, constructing the global frame. Nevertheless, as the number of measurement station increases, a long coordinate system transformation chain will lead to severe error accumulation [6, 7]. In addition, LTs can only perform single-target measurement and requires manual assistance in multi-target measurement tasks, which greatly extends the operation process. Therefore, single-station measurement systems fail to meet the requirements on accuracy and collaborative measurement ability in advanced equipment manufacturing.

The integral multi-station measurement system represented by indoor GPS (iGPS), workshop Measuring and Positioning System (wMPS) or a multi-camera system, is becoming increasingly popular in in the past decade [8–11]. They can measure the position or pose of multiple targets based on the principle of multi-observation intersection, as shown in the blue zone in figure 1. Compared with the single-station measurement system, the integral multi-station measurement system uses a unified spatial and temporal reference to network all measurement stations (more than two stations), constructing a high-precision, extensible measurement field without error accumulation [12]. This characteristic is beneficial for the integral multi-station measurement system to demonstrate outstanding potentials in large-scale manufacturing scenes [13–15].

However, owing to the principle of intersection measurement, the measurement precision control in an integral multi-station measurement system is much more difficult than a single-station measurement system. The key point for intersection measurement is to construct the geometry constraints. They usually consist of angle and length observations from the measurement stations that are involved in measurement. The constraint strength determines the sensitivity of the measurement error to the station observation errors [16, 17]. Nevertheless, due to the different positions of the measured target in the field or the loss of line of sight, the geometry constraints in an integral multi-station measurement field are changing during measurements and this leads to complicated error characteristics. According to the redundancy of geometry constrains, we discuss the change of geometry constraints using figure 2. When the target is in the unmeasurable zone (only one station can measure the target), the geometry constraints are insufficient and it is not able to solve the coordinate or pose,

causing measurement interruption. In the other area where the geometry constraints are redundant (i.e. two or more stations are involved in measurements), when the spatial occlusion occurs or the measured target crosses the boundary of some stations, the transmitters that emit signals to a receiver will change, leading to corresponding change in geometry constraint and spatially non-continuous error. To point out, due to that the unmeasurable area can be effectively avoided by optimizing the layout of the measurement stations, we are more interested in the spatially non-continuous error when geometry constraints change. This is the main topic of our paper.

The approach for reducing and compensating the non-continuous error of the integral multi-station measurement system can be summarized into two categories:

(1) According to the characteristic of intersection measurement, the intersection stability is used to evaluate the stability of the solution (measurement result). By improving the intersection stability of constraint equations, the non-continuous change in measurement errors can be partly corrected. In the existing research, the intersection stability is often summarized as a mathematical parameter represented by the condition number of the parameter matrix formed by all geometry constraint equations. In [18–20], methods are presented to decrease the condition number by transforming the measurement model and regularizing the observation matrix, improving the stability of the solution. However, these methods overlook the metrology property of the constraint stability, and the corrected solution may not be globally optimal, failing to gain a satisfying result in actual engineering applications.

(2) To restore the spatial continuity in consecutive measurements, auxiliary measurement systems are introduced to provide prior motion knowledge and spatial continuity In [21–23] and [24–26], light detection and ranging and inertial measurement unit (IMU) are introduced to improve the measurement performance of the vision measurement system in weak texture conditions. This method is widely used in automatic driving, control of UAV and other scenarios. Lukas *et al* from Eidgenössische Technische Hochschule Zürich (ETH) proposed a method that integrating iGPS and IMU for the positioning of industrial robots [27]. The robot moved along a 1.2 m long straight line inbetween the two taught points. After error correction, the errors are dominantly lower than 0.5 mm. All applications mentioned above can be expressed as the performance complements of the integral multi-station measurement system and auxiliary instrument. The integral multi-station measurement system compensates the spatial scale drift error or time accumulation error of the auxiliary system periodically, and the auxiliary instrument helps to compensate the positioning error of the integral multi-station measurement system [28, 29]. However, in the existing research above, there is few research on dynamic error modeling and compensation. What's worse, the non-continuous error is also not modeled and evaluated. As a result, the accuracy control strategy is incomprehensive,
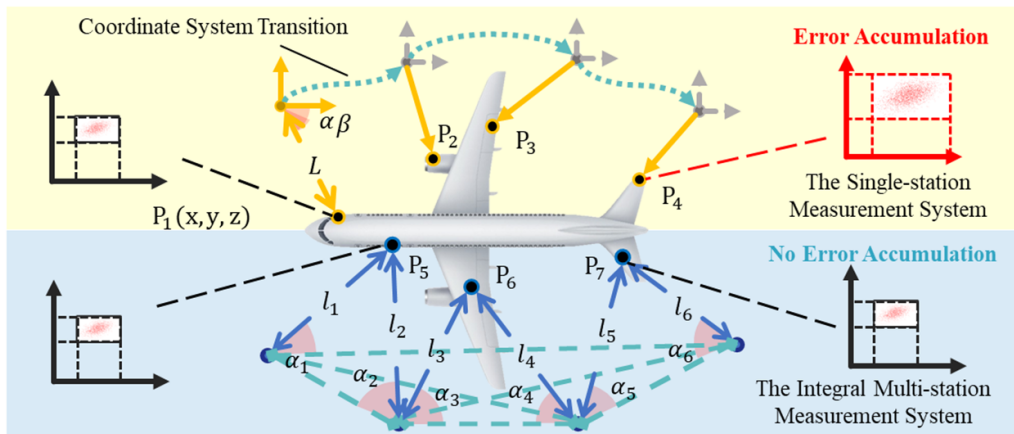
Figure 1. Comparison of a single-station measurement system and an integral multi-station measurement system.
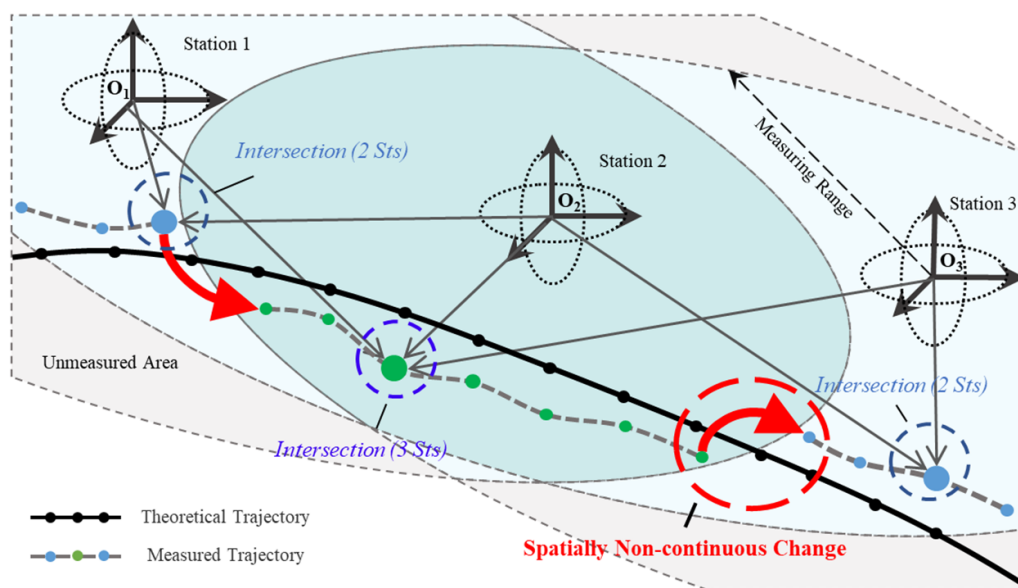

Figure 2. Non-continuous error caused by the change of geometry constraint.

failing to gain satisfying global accuracy. This is the main drawback of the methods above.

wMPS has similar measurement principle as iGPS and is widely utilized in large-scale metrology [30, 31]. wMPS consists of rotary scanning transmitters, photoelectric receivers and the signal processor. By networking multiple transmitters, we can construct an extensible, high-precision measurement field [32, 33]. As a typical integral multi-station measurement system, the non-continuous error caused by the change of geometry constraints is also an unsolved problem for wMPS and limits its performance. As a result, wMPS is an ideal platform for studying the non-continuous error. In previous experiments and applications, we found that the non-continuous error is especially significant when the number of stations in the measurement filed increases or there is spatial occlusion in complicated environment, failing to fully develop the potentials of these systems in large-scale metrology. It is the main motivation of our research.

In this paper, we first analyze the generation mechanism and characteristics of the spatially non-continuous error of the integral multi-station measurement system and propose the mathematical model. Secondly, we take wMPS as the research platform and present a method that combining the Guide to the Expression of Uncertainty in Measurement (GUM) method and measurement model of wMPS to evaluate the significance of the non-continuous error. This is the key point to effectively identify the non-continuous error and serves as the pre-work and foundation for our future work to compensate the non-continuous error. To our best knowledge, this is the first systematic research to propose the concept, analyze the generation mechanism and then evaluate the significance of non-continuous error.

The rest of this paper is organized as follows: in section 2 the definition and generation mechanism of the non-continuous error are presented. In section 3 the significance of the non-continuous error is analyzed, and an evaluation criterion is given. In section 4 the simulations and verification
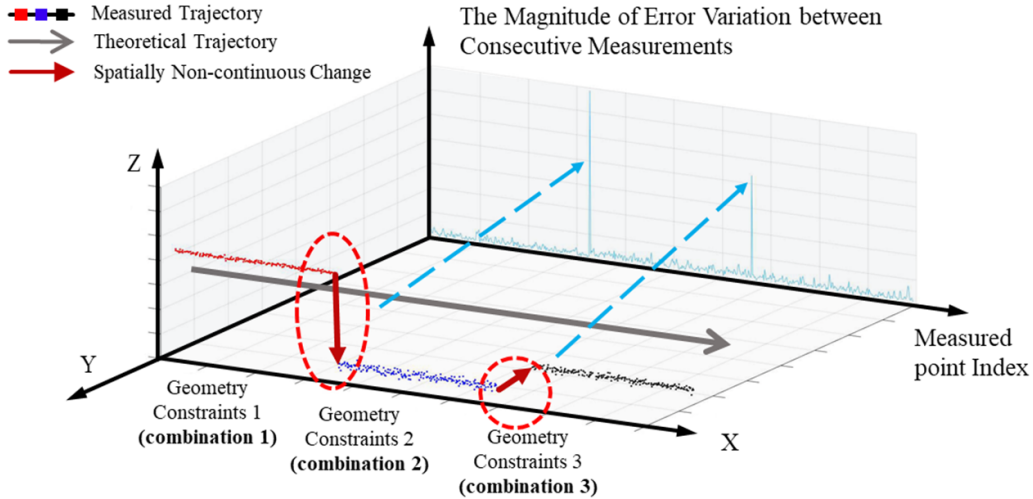
Figure 3. Non-continuous error in a linear trajectory measurement.

experiments are designed and carried out. In section 5 the conclusions are presented along with a brief overview for our future research.

2. Definition and generation mechanism of non-continuous error

2.1. Definition of non-continuous error

In the integral multi-station measurement field, the coordinates sequence derived from consecutive measurements describes the trajectory of the target. In most cases, the real motion trajectory of the target is spatially smooth and continuous. As a result, the sequence of the coordinates should be continuous numerically as well. However, when the geometry constraints change (different combinations of measurement stations) as described in figure 2, there will be non-continuous error in consecutive measurements that cannot be avoided.

We use figure 3 for further clarification. The theoretical trajectory and the measured trajectory formed by discrete measured points are shown on the front side. According to the geometry constraints, the measured trajectory is divided into three segments that are represented by different colors. The deviation between each measured point and the theoretical point is defined as the measurement error. When the geometry constraint changes, there will be significant change in the measurement error (dashed circles). We calculate the error variations between every two consecutive measurements and show the magnitudes on the back side of figure 3. It is worth noting that the magnitude of error variation is small in each continuous segment but dramatically large when the geometry constraint changes.

As shown in figure 4, measurement error e_k is the deviation between measurement $\mathbf{X}_k$ and its true value $\widehat{\mathbf{X}}_k$. The consecutive measurements $\{\mathbf{X}_1, \ldots, \mathbf{X}_k\}$ and consecutive measurements $\{\mathbf{X}_{k+1}, \ldots, \mathbf{X}_m\}$ are derived from different combinations of multiple stations and they have their respective geometry

constraint. The error variation between two consecutive measurements are all within a narrow error envelope of $e^{\theta, \mathbf{l}}$. Since the error propagation model is related to the geometry constraints, for the two consecutive measurements $\mathbf{X}_k$, $\mathbf{X}_{k+1}$ that are related with different geometry constraints, the change of geometry constraints will result in significant change in measurement errors e_k and e_{k+1}.

As mentioned above, the magnitude of error variation between two consecutive measurements shows the spatial non-continuity of the measured trajectory. We define the spatially non-continuous error e_C as the error difference between two consecutive measurements that have different geometry constraints, as shown in equation (1):

$$e_C = e_{k+1} - e_k. \tag{1}$$

2.2. Generation mechanism of non-continuous error

To analyze the generation mechanism of the non-continuous error, a general measurement model of the intersection measurement is depicted as shown in figure 5.

According to the principle of intersection measurement, the geometry constraint is constructed with the observations of angle and length observations to calculate the coordinate of the measured point, as shown in equation (2):

$$f(\{\boldsymbol{\theta}, \mathbf{l}\}, \{\mathbf{R}|\mathbf{T}\}, \mathbf{X}) = 0 \tag{2}$$

where $\boldsymbol{\theta}, \mathbf{l}$ denotes the length and angle observations of different measurement stations. Generally, the observations of all measurement stations are well calibrated and the systematic error in observations is well corrected. The random error in observations from different stations is the main error source. Therefore, the error in the observation of a single station is simplified as a random error. $\mathbf{R}|\mathbf{T}$ are the extrinsic parameters of stations that are obtained through a calibration process [34]. Since the extrinsic parameters are constant in the measurement process, their errors are regarded as systematic errors. $\mathbf{X}$ is the coordinate of the measured point.
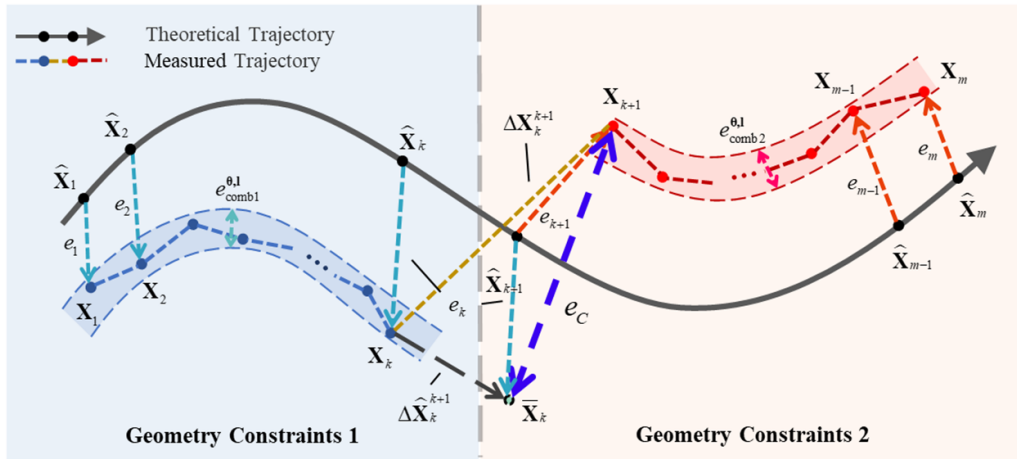
Figure 4. Non-continuous error envelopes caused by different geometry constraints.
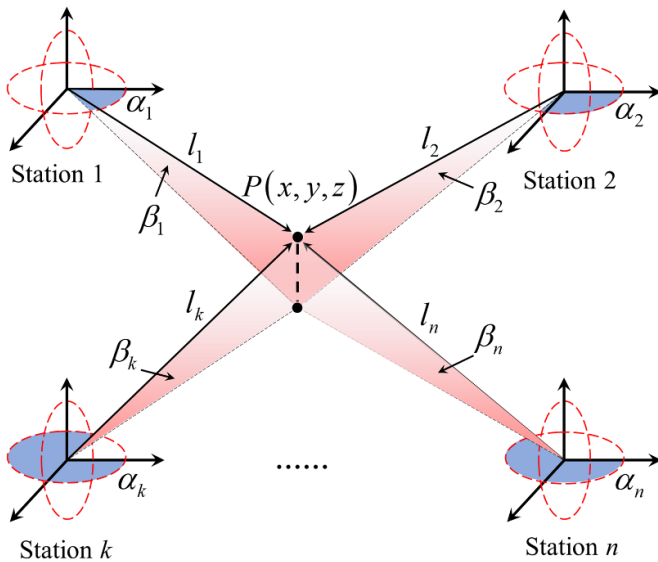

Figure 5. General measurement model of intersection measurement in an integral multi-station measurement system.

The two factors, i.e. the random observation error and extrinsic parameter error of each station, are related to the positioning error of the integral multi-station measurement system. The random error of station observation $\{\Delta\boldsymbol{\theta}, \Delta\mathbf{l}\}$ obeys a normal distribution $N(\mu, \sigma)$. As shown in figure 6, for every single measurement, the propagated measurement error $e^{\boldsymbol{\theta}, \mathbf{l}}$ follows an ellipsoidal error distribution. The shape and pose of the ellipsoid is determined by the geometry constraints [7]. When we only take the random errors of the station observation into account, the center lines of measurement errors are collinear no matter how drastically the error envelopes change for the two measured trajectory segments with different geometry constraints (figure 7(a)). As a result, the error envelopes always overlap, which means the two segments should be regarded as continuous and we are not able to identify the non-continuous error. Therefore, we draw the conclusion that the

errors in the station observations are not dominant in the generation of non-continuous error although the geometry constraint changes.

The extrinsic parameter error $\Delta\mathbf{R}_n | \Delta\mathbf{T}_n$ of multiple stations represents the deviation between the extrinsic parameter of station n $\mathbf{R}_n | \mathbf{T}_n$ derived from the calibration process and their true values $\widehat{\mathbf{R}}_n | \widehat{\mathbf{T}}_n$. If we take both the random error of station observation and the extrinsic parameter error into account, the error envelopes will separate and there will be a significant jump when the geometry constraint (combination of stations involved in measurement) change (figure 7(b)). Here we use figure 8 as the example for further clarification. The observations from stations 1, 2 and 3 strictly intersect at $\widehat{\mathbf{X}}_k$. Influenced by the extrinsic parameter error, the ideal intersection is disturbed and they re-intersect at an optimal point $\mathbf{X}_k$ (derived from the measurement model). The measurement error of kth measurement $e_k^{\mathbf{R}|\mathbf{T}}$ under the influence of $\Delta\mathbf{R}|\Delta\mathbf{T}$ can be described in equation (3):

$$e^{\mathbf{R}|\mathbf{T}} = \mathbf{X} - \widehat{\mathbf{X}} = g(\Delta\mathbf{R}|\Delta\mathbf{T}), \Delta\mathbf{R}|\Delta\mathbf{T} = \begin{bmatrix} \Delta\mathbf{R}_1|\Delta\mathbf{T}_1 \\ \vdots \\ \Delta\mathbf{R}_n|\Delta\mathbf{T}_n \end{bmatrix}.$$
(3)

For two consecutive measurements $\mathbf{X}_k$ and $\mathbf{X}_{k+1}$ as shown in figure 8, their geometry constraint or combination of measurement stations are different. This may lead to significant change in measurement errors. To sum up, we can conclude that the extrinsic parameter errors would affect the spatial continuity of measurement errors when the geometry constraint changes.

3. Evaluating the significance of non-continuous error

As defined in section 2, the non-continuous error refers to the change in the errors between two consecutive measurements with distinct geometry constraints, and it is mainly
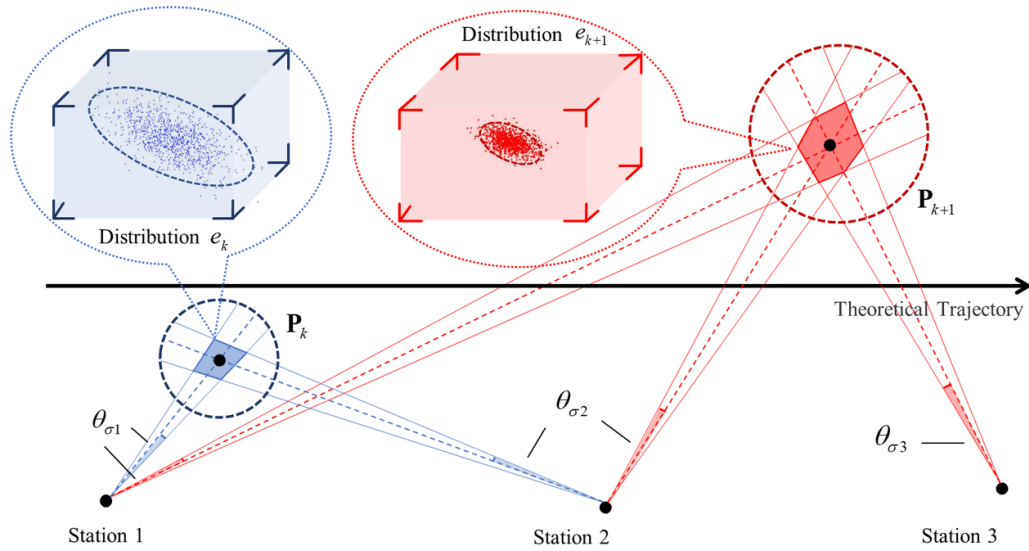
Figure 6. Different ellipsoidal error distributions derived from different geometry constraints.
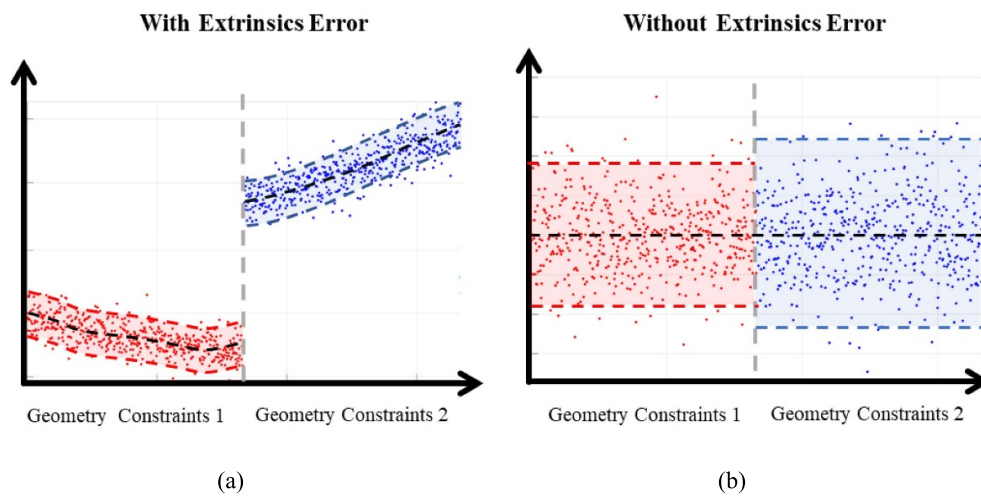

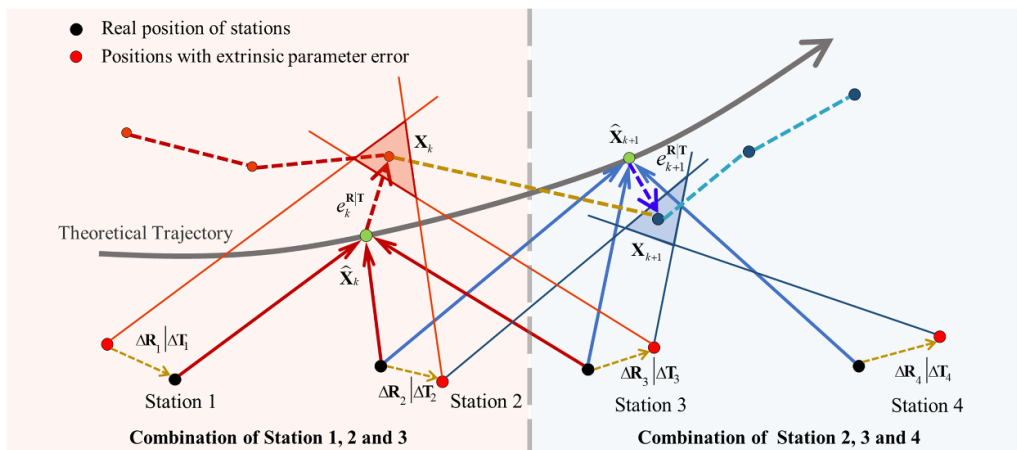**Figure 7.** Error distribution without/with extrinsic parameter errors of multiple stations.

Figure 8. The influence of extrinsic parameter error on the continuity of measurement errors when the geometry constraint changes.
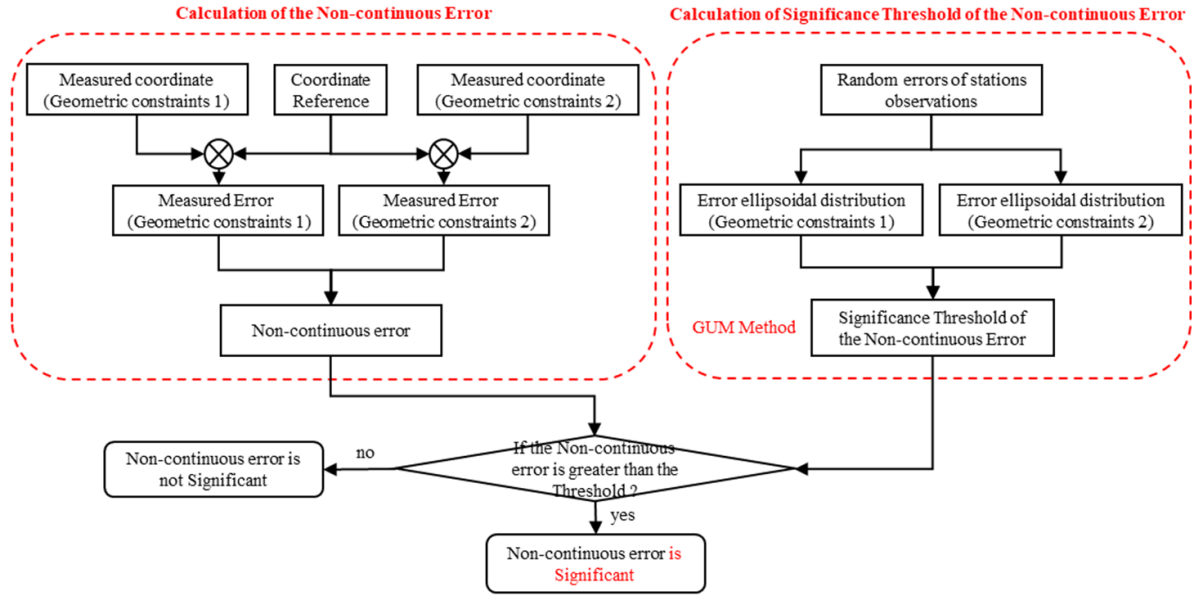
Figure 9. The workflow chart of the proposed method.

determined by the extrinsic parameter errors of multiple stations. When the norm of the non-continuous error is smaller than the random error, it will be merged and is not significant. In this section, a method to evaluate the significance of non-continuous errors is proposed. Firstly, the non-continuous error is modeled to define the significance in consecutive measurements. Secondly, we combine the GUM method and the measurement model of wMPS to generated the ellipsoidal error distributions of two consecutive measurements. The threshold for significance evaluation is obtained by superposing the lengths of both long axes. The flowchart of the proposed method is shown in figure 9.

3.1. Significance criterion of non-continuous error

According to the definition in section 2.1, the non-continuous error of consecutive measurements $\mathbf{X}_k$ and $\mathbf{X}_{k+1}$ is described as the difference between their measurement errors, as shown in equation (1). Considering that e_k is difficult to obtain directly, we prefer to use the optimal estimation of the measurement $\widetilde{\mathbf{X}}_k$ to replace its true value $\widehat{\mathbf{X}}_k$. Equation (1) can be rewritten as equation (4):

$$
\begin{aligned}
e_C = e_{k+1} - e_k &= \left(\mathbf{X}_{k+1} - \widehat{\mathbf{X}}_{k+1}\right) - \left(\mathbf{X}_k - \widehat{\mathbf{X}}_k\right) \\
&= \left(\mathbf{X}_{k+1} - \mathbf{X}_k\right) - \left(\widehat{\mathbf{X}}_{k+1} - \widehat{\mathbf{X}}_k\right) \\
&= \left(\mathbf{X}_{k+1} - \mathbf{X}_k\right) - \left(\widetilde{\mathbf{X}}_{k+1} - \widetilde{\mathbf{X}}_k\right). \quad (4)
\end{aligned}
$$

As shown in figure 10, the norm of non-continuous error e_C can be regarded as the distance between two consecutive measurements k and $k+1$. When the norm of the non-continuous error is larger than the maximum distance between the two error ellipsoids, there is no overlapping area between the two

distributions and the measured trajectory is therefore not continuous. The non-continuous error is significant in this case.

Therefore, the threshold of the significance criterion is defined as twice the sum of error ellipsoid radius along the direction of vector $\boldsymbol{n}$, as shown in equation (5). $\boldsymbol{n}$ is determined by the centers of the two error ellipsoids. On the contrary, if the norm of the non-continuous error is less than the threshold, it is not significant and cannot be effectively identified

$$
e_{\text{thres}} = 2\left(\left\|\mathbf{R}_k^{e^{\Delta\theta}}\right\|^2 + \left\|\mathbf{R}_{k+1}^{e^{\Delta\theta}}\right\|^2\right). \quad (5)
$$

3.2. Method to calculate the threshold of the significance criterion

To calculate the threshold of the significance criterion, we first calculate the radius the error distribution ellipsoids corresponding to the consecutive measurements $\mathbf{X}_k$ and $\mathbf{X}_{k+1}$. The error ellipsoid can be expressed using the measurement uncertainty matrix $u_k^{\Delta\theta}$ and $u_{k+1}^{\Delta\theta}$ as equation (6):

$$
u_k^{\Delta\theta} = \begin{bmatrix} u^2(x_k) & u(x_k,y_k) & u(x_k,z_k) \\ u(y_k,x_k) & u^2(y_k) & u(y_k,z_k) \\ u(z_k,x_k) & u(z_k,y_k) & u^2(z_k) \end{bmatrix},
$$

$$
u_{k+1}^{\Delta\theta} = \begin{bmatrix} u^2(x_{k+1}) & u(x_{k+1},y_{k+1}) & u(x_{k+1},z_{k+1}) \\ u(y_{k+1},x_{k+1}) & u^2(y_{k+1}) & u(y_{k+1},z_{k+1}) \\ u(z_{k+1},x_{k+1}) & u(z_{k+1},y_{k+1}) & u^2(z_{k+1}) \end{bmatrix}
$$

(6)

where $u(x,y)$ is the covariance of the coordinates of x and y. Due to that the random error of each observation is independent to any other and obeys the normal distribution $N\left(\mu,\sigma^2\right), \mu = 0$, the covariance matrix of the observation errors $u_{\Delta\theta}$ is obtained as equation (7):

$$u_{\Delta\theta} = \begin{bmatrix} \sigma_{11}^2 & 0 & \cdots & 0 \\ 0 & \sigma_{12}^2 & \cdots & 0 \\ \vdots & \vdots & \ddots & \vdots \\ 0 & 0 & \cdots & \sigma_{n2}^2 \end{bmatrix} \qquad (7)$$

where σ_{n1}^2, σ_{n2}^2 represent the variance of the observation error of the *n*th station.

According to the propagation law of measurement uncertainty, the measurement uncertainty matrix $u_k^{\Delta\theta}$ and $u_{k+1}^{\Delta\theta}$ can be calculated when taking the covariance matrix $u_{\Delta\theta}$ as the input, as shown in equation (8):

$$u_k^{\Delta\theta} = \frac{d\mathbf{X}_k}{d\theta} u_{\Delta\theta} \left(\frac{d\mathbf{X}_k}{d\theta}\right)^{\mathrm{T}} \qquad (8)$$

where $\frac{d\mathbf{X}}{d\theta}$ is the sensitivity matrix consisting of all the first partial derivatives $\frac{\partial \mathbf{X}_i}{\partial \theta_i}$. The sensitivity matrix is shown in equation (9):

$$\frac{d\mathbf{X}}{d\theta} = -\left(\frac{dF}{d\mathbf{X}}\right)^+ \frac{dF}{d\theta}, \frac{d\mathbf{X}}{d\theta} = \begin{bmatrix} \frac{\partial x}{\partial \theta_{11}} & \frac{\partial y}{\partial \theta_{11}} & \frac{\partial z}{\partial \theta_{11}} \\ \frac{\partial x}{\partial \theta_{12}} & \frac{\partial y}{\partial \theta_{12}} & \frac{\partial z}{\partial \theta_{12}} \\ \frac{\partial x}{\partial \theta_{21}} & \frac{\partial y}{\partial \theta_{21}} & \frac{\partial z}{\partial \theta_{21}} \\ \vdots & \vdots & \vdots \\ \frac{\partial x}{\partial \theta_{n2}} & \frac{\partial y}{\partial \theta_{n2}} & \frac{\partial z}{\partial \theta_{n2}} \end{bmatrix} \qquad (9)$$

where $\left(\frac{dF}{d\mathbf{X}}\right)^+$ is the generalized inverse matrix of the sensitivity matrix $\frac{dF}{d\mathbf{X}}$. $\frac{dF}{d\mathbf{X}}$ and $\frac{dF}{d\theta}$ are the Jacobian matrices of *F* and **X**, respectively. The Eigen-decomposition of $u_k^{\Delta\theta}$ is shown in equation (10):

$$u_k^{\Delta\theta} = \mathbf{r}\mathbf{u}_{\mu\nu\eta}\mathbf{r}^{\mathrm{T}} = \begin{bmatrix} \boldsymbol{\mu} & \boldsymbol{\nu} & \boldsymbol{\eta} \end{bmatrix} \begin{bmatrix} u^2(\mu) & 0 & 0 \\ 0 & u^2(\nu) & 0 \\ 0 & 0 & u^2(\eta) \end{bmatrix} \begin{bmatrix} \boldsymbol{\mu}^{\mathrm{T}} \\ \boldsymbol{\nu}^{\mathrm{T}} \\ \boldsymbol{\eta}^{\mathrm{T}} \end{bmatrix} \qquad (10)$$

where the $\boldsymbol{\mu}$, $\boldsymbol{\nu}$ and $\boldsymbol{\eta}$ are orthogonal unit eigenvectors. $u^2(\mu)$, $u^2(\nu)$ and $u^2(\eta)$ are corresponding eigenvalues.

The three axes of error ellipsoid are parallel to eigenvectors, and the radius are $ku(\mu)$, $ku(\nu)$ and $ku(\eta)$ ($k = 2.8$). **r** represents the pose matrix of the error ellipsoid distribution. By normalizing the displacement between the measurements $\mathbf{X}_k$ and $\mathbf{X}_{k+1}$, we can get vector as $\mathbf{n} = \begin{bmatrix} \mathbf{n_x} & \mathbf{n_y} & \mathbf{n_z} \end{bmatrix}$. Because the size of the error ellipsoids is negligible when compared to the target motion, the vector **n** can be regarded as the direction determined by the two error ellipsoids centers. $\mathbf{R}_k^{e^{\Delta\theta}}$ in figure 10 can be represented by the projection of the error ellipsoid axes along the direction of vector **n**. Its length is calculated as equation (11):

$$\left\| \mathbf{R}_k^{e^{\Delta\theta}} \right\|^2 = \begin{bmatrix} \mathbf{n_x} & 0 & 0 \\ 0 & \mathbf{n_y} & 0 \\ 0 & 0 & \mathbf{n_z} \end{bmatrix} \left(\mathbf{r} \begin{bmatrix} ku(\mu) & ku(\nu) & ku(\eta) \end{bmatrix}^{\mathrm{T}} \right). \qquad (11)$$

Therefore, the threshold of significance criterion for the non-continuous error can be calculated.
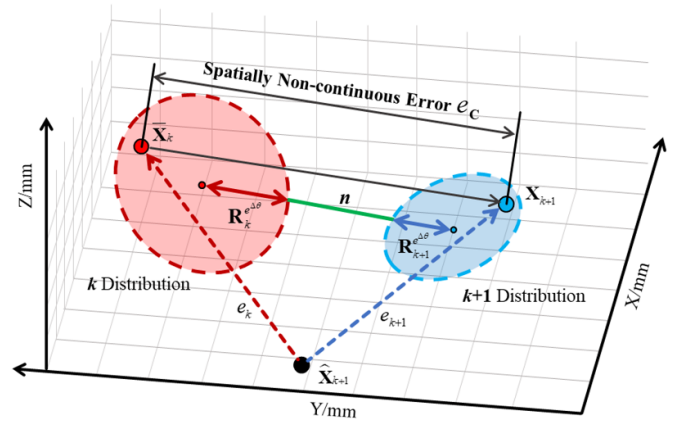

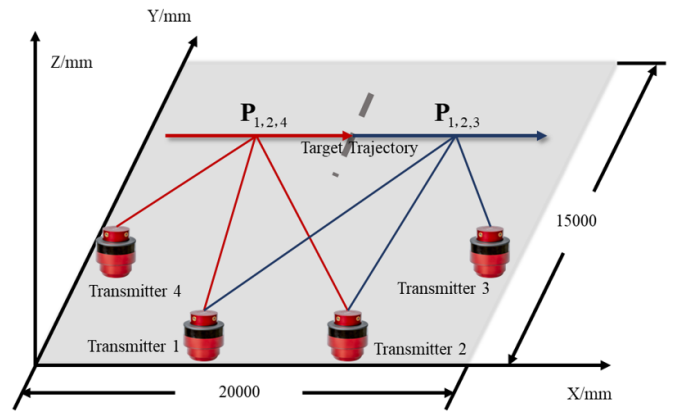**Figure 10.** The schematic of the significance criterion of the non-continuous error.

Figure 11. The layout of wMPS measurement field in simulations.

4. Simulations and experiments

4.1. Simulation results and analysis

In order to evaluate the effectiveness of the significance criterion comprehensively, two simulations are carried out to show the performance when the non-continuous error is significant and not significant, respectively. The simulation set-up is shown in figure 11.

There are four wMPS transmitters that locate in a measurement volume of 20 m × 15 m × 3 m with a 'C' type layout. We set 500 measurement points along the trajectory with an equal interval. These measurement points are divided into two groups: the first group includes measurement points 1–250, and they are measured by transmitters 1, 2 and 4. Points 251–500 belong to the second group and they are measured by transmitters 1, 2 and 3. For each point, the nominal angle measurements of all transmitters are calculated. The uncertainty of angle measurement for each transmitter is set as 1.7″.

In the first simulation, the pose error and the translation error of each transmitter (extrinsic parameter error) are set as 5″ and 0.5 mm to make the non-continuous error significant. In the second simulation, the extrinsic parameter errors are set
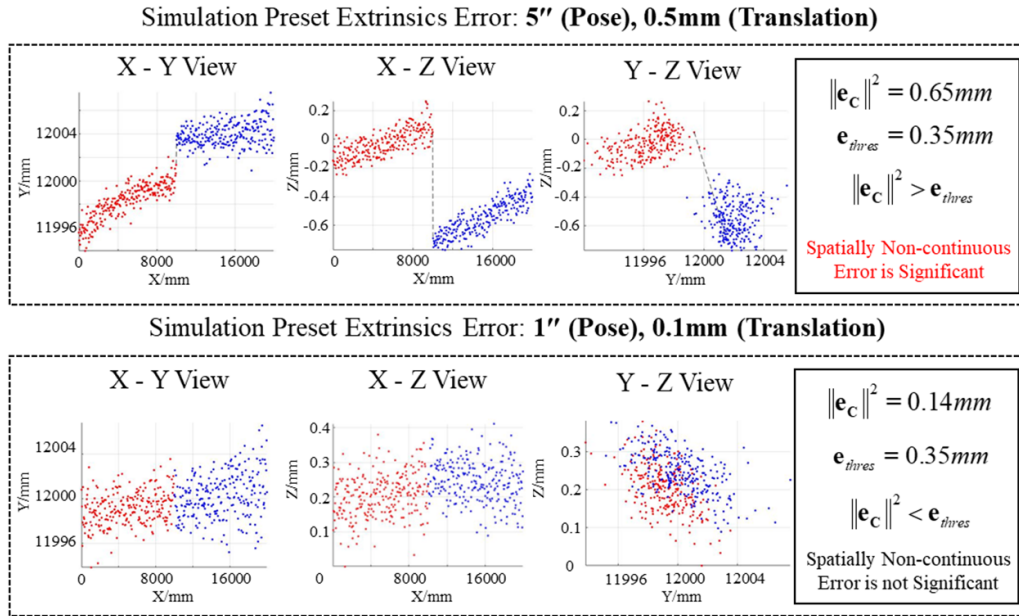
Figure 12. Simulation results from different presets.

as $1''$ and 0.1 mm to make it insignificant. By using the Monte-Carlo Method, the coordinates of all measured points are calculated, and the non-continuous errors in two simulations are calculated. We then calculate the threshold and evaluate the significance using the criterion presented in section 3.2.

The results of simulations are shown in figure 12. In the first simulation, the norm of non-continuous errors is 0.65 mm and the threshold is 0.35 mm. The norm of non-continuous error is larger than the threshold and it is significant. In the second simulation, the norm of the non-continuous errors is 0.14 mm and the threshold is 0.35 mm. As a result, the non-continuous error is not significant. The results in both simulations are consistent with our presets, verifying the effectiveness of significance criterion.

4.2. Experiment results and analysis

In order to further verify the effectiveness of significance criterion in physical measurement, we designed an experiment basing on wMPS. The experimental setup is shown in figure 13. Four transmitters are deployed in a 'C' type layout with an interval of 4 m–5 m. An LT is employed as the reference system. The measured target consists of a 1.5 inch magnetic nests, a wMPS receiver and a LT reflector. They are placed on the platform of a linear guide.

Since the wMPS receiver has the same size as the LT reflector, it is convenient to use LT to provide high accuracy references by exchanging the wMPS receiver and reflector. We first construct a point network with LT and calibrate the extrinsic parameters of four transmitters using the network, aligning the coordinate frames of wMPS and LT. The length of the movement alone the linear guide is 924.85 mm and the interval between the consecutive measurement points is about

25 mm. We get the coordinates of the receiver from wMPS and its reference value from LT at 38 points.

Due to limited space in our laboratory and the fact that each transmitter used in this experiment has a measurement range over 20 meters, all transmitters can easily cover the entire volume. This makes it difficult to replicate the change in geometry constraints. To overcome this limitation and validate our proposed method, an allocation strategy was applied to pre-set the transmitters used in the measurement of each segment. The signals from transmitters that are out of selection will not be used for calculation. In this experiment the points of four segments are calculated by the angle observations from transmitter 1 and 2, 2 and 3, 3 and 4, 1 and 4, respectively. Besides, in order to fully validate the proposed method, we performed several groups of experiments by placing the linear guide at different positions and orientations in the measurement field and get considerable results among all groups. We only show the representative result in one group in this paper for simplicity.

We calculate the non-continuous errors of the four segments at the boundary point. Their magnitudes are 0.39 mm, 1.16 mm and 1.08 mm, and the thresholds of significance criterion in this case are 0.23 mm, 0.40 mm and 0.28 mm. They are all significant, which matches well with the errors when compared with LT, as shown in figure 14. The effectiveness of significance criterion is well verified.

We further clarify that the linear guide in this experiment only works as the carrier for the measured target and generates a spatial trajectory to change of the target position. We only pay attention to the result of the movement, i.e. the change in positions, but not the process of the movement. As a result, the movement state such as the trajectory or the speed has no influence on the performance of the proposed method. Our method has the potential to be utilized in the measurement of complicated movement.
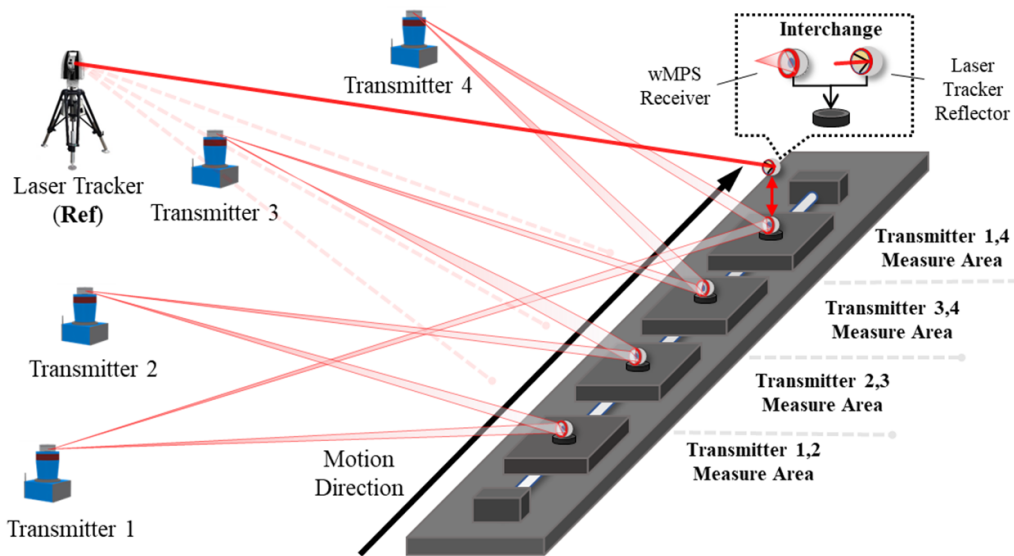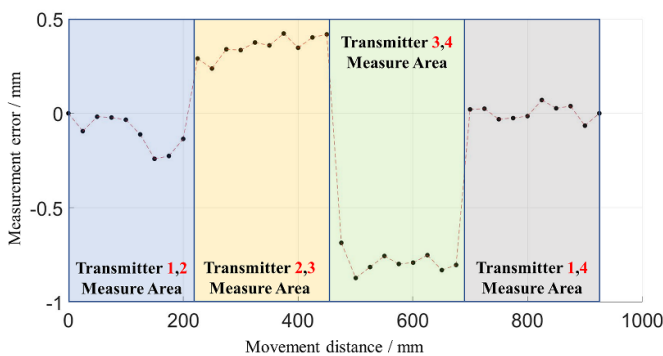
Figure 13. Experimental set-up with wMPS and LT.

Figure 14. Measurement errors of 38 points along a linear trajectory.

5. Conclusions

This paper focuses on the non-continuous error of the integral multi-station measurement system. We define non-continuous error as the error deviation between two consecutive measurements that are related with different geometry constraints or combinations of measurement stations. Then we analyze the generation mechanism of non-continuous error and demonstrate the relationship between the spatial continuity and extrinsic parameter errors. To identify the non-continuous error for further compensation, the significance criterion is proposed. Then a GUM-based method is presented to calculate the threshold for evaluating the significance of the non-continuous error. To verify the effectiveness of the significance criterion, simulations and experiments are designed and carried out. The simulation results are consistent with our presets and the experimental results matches well with the reference from LT, which verifies the effectiveness of the significance criterion both in the principle level and application level.

With regard to the compensation of the non-continuous error, more detailed research is to be carried out in the future.

This may include the research on a calibration based method for controlling the extrinsic parameter errors, and an optimization framework for compensating the non-continuous error.

Data availability statement

All data that support the findings of this study are included within the article (and any supplementary files).

Acknowledgments

ORCID iDs

Shendong Shi ⬥ https://orcid.org/0000-0002-2490-0578
Linghui Yang ⬥ https://orcid.org/0000-0002-9937-1383

References

[1] Zhou J, Li P, Zhou Y, Wang B, Zang J and Meng L 2018 Toward new-generation intelligent manufacturing *Engineering* **4** 11–20
[2] Wang B, Tao F, Fang X, Liu C, Liu Y and Freiheit T 2021 Smart manufacturing and intelligent manufacturing: a comparative review *Engineering* **7** 738–57
[3] Zhou J 2013 Digitalization and intelligentization of manufacturing industry *Adv. Manuf.* **1** 1–7
[4] Li C, Zheng P, Li S, Pang Y and Lee C K M 2022 AR-assisted digital twin-enabled robot collaborative manufacturing system with human-in-the-loop *Robot. Comput.-Integr. Manuf.* **76** 102321

[5] Schmitt R H, Peterek M, Morse E, Knapp W, Galetto M, Härtig F, Goch G, Hughes B, Forbes A and Estler W T 2016 Advances in large-scale metrology- review and future trends *CIRP Ann.* **65** 643–65

[6] Yang Y and Xu T 2002 Combined method of datum transformation between different coordinate systems *Geo-Spat. Inf. Sci.* **5** 5–9

[7] Ren Y, Lin J, Zhu J, Sun B O and Ye S 2015 Coordinate transformation uncertainty analysis in large-scale metrology *IEEE Trans. Instrum. Meas.* **64** 2380–8

[8] Gao W, Kim S, Bosse H, Haitjema H, Chen Y L, Lu X D, Knapp W, Weckenmann A, Estler W T and Kunzmann H 2015 Measurement technologies for precision positioning *CIRP Ann.* **64** 773–96

[9] Zeng Q, Huang X, Li S and Deng Z 2019 High-efficiency posture prealignment method for large component assembly via iGPS and laser ranging *IEEE Trans. Instrum. Meas.* **69** 5497–510

[10] Puerto P, Leizea I, Herrera I and Barrios A 2023 Analyses of key variables to industrialize a multi-camera system to guide robotic arms *Robotics* **12** 10

[11] Chen F, Chen X, Xie X, Feng X and Yang L 2013 Full-field 3D measurement using multi-camera digital image correlation system *Opt. Lasers Eng.* **51** 1044–52

[12] Wang D, Tang W and Zhang X Ma Q, Wang J, Sun H and Shao J 2015 A universal precision positioning equipment in coordinate unified for large scale metrology *2015 IEEE Int. Conf. on Mechatronics and Automation (ICMA)* (IEEE) pp 1761–6

[13] Wang Z, Mastrogiacomo L, Franceschini F and Maropoulos P 2011 Experimental comparison of dynamic tracking performance of iGPS and laser tracker *Int. J. Adv. Manuf. Technol.* **56** 205–13

[14] Robson S, MacDonald L, Kyle S, Boehm J and Shortis M 2018 Optimised multi-camera systems for dimensional control in factory environments *Proc. Inst. Mech. Eng.* B **232** 1707–18

[15] Storm C, Hose H and Schmitt R H 2021 State estimation and model-predictive control for multi-robot handling and tracking of AGV motions using iGPS *2021 IEEE/RSJ Int. Conf. on Intelligent Robots and Systems (IROS)* (IEEE) pp 1038–45

[16] Zafari F, Gkelias A and Leung K 2019 A survey of indoor localization systems and technologies *IEEE Commun. Surv. Tutor.* **21** 2568–99

[17] Li M, Jiang F and Pei C 2020 Review on positioning technology of wireless sensor networks *Wirel. Pers. Commun.* **115** 2023–46

[18] Mascotto L 2018 Ill-conditioning in the virtual element method: stabilizations and bases *Numer. Methods Partial Differ. Equ.* **34** 1258–81

[19] Antunes P 2018 A numerical algorithm to reduce ill-conditioning in meshless methods for the Helmholtz equation *Numer. Algorithms* **79** 879–97

[20] Beik F, Jbilou K, Najafi-Kalyani M and Reichel L 2020 Golub-Kahan bidiagonalization for ill-conditioned tensor equations with applications *Numer. Algorithms* **84** 1535–63

[21] Park K, Kim S and Sohn K 2019 High-precision depth estimation using uncalibrated LiDAR and stereo fusion *IEEE Trans. Intell. Transp. Syst.* **21** 321–35

[22] Graeter J, Wilczynski A and Lauer M 2018 LIMO: LiDAR-monocular visual odometry *2018 IEEE/RSJ Int. Conf. on Intelligent Robots and Systems (IROS)* (IEEE) 7872–9

[23] Seo Y and Chou C 2019 A tight coupling of vision-LiDAR measurements for an effective odometry *2019 IEEE Intelligent Vehicles Symp. (IV)* (IEEE) pp 1118–23

[24] Campos C, Elvira R, Rodríguez J, Montiel J M M and Tardos J D 2021 ORB-SLAM3: an accurate open-source library for visual, visual-inertial, and multimap SLAM *IEEE Trans. Robot.* **37** 1874–90

[25] Yang Y, Geneva P and Zuo X Eckenhoff K, Liu Y, and Huang G 2019 Tightly-coupled aided inertial navigation with point and plane features *2019 Int. Conf. on Robotics and Automation (ICRA)* (IEEE) pp 6094–100

[26] Schubert D, Goll T and Demmel N V Usenko J Stückler, and Cremers D 2018 The TUM VI benchmark for evaluating visual-inertial odometry *2018 IEEE/RSJ Int. Conf. on Intelligent Robots and Systems (IROS)* (IEEE) pp 1680–7

[27] Stadelmann L, Sandy T, Thoma A and Buchli J 2019 End-effector pose correction for versatile large-scale multi-robotic systems *IEEE Robot. Autom. Lett.* **4** 546–53

[28] Qin T, Li P and Shen S 2018 VINS-Mono: a robust and versatile monocular visual-inertial state estimator *IEEE Trans. Robot.* **34** 1004–20

[29] Han S, Deng F and Li T and Pei H 2022 Tightly coupled optimization-based GPS-visual-inertial odometry with online calibration and initialization (arXiv:2203.02677)

[30] Xiong Z, Zhu J, Yang X, Papasian C J, Wang J Q, Xiong Z G and Chu X P 2011 A novel laser multidirection network measurement system *2011 2nd Int. Conf. on Digital Manufacturing and Automation* (IEEE) pp 89–92

[31] Zhao Z, Zhu J, Lin J, Yang L, Xue B and Xiong Z 2014 Transmitter parameter calibration of the workspace measurement and positioning system by using precise three-dimensional coordinate control network *Opt. Eng.* **53** 084108

[32] Guo S, Lin J, Ren Y, Yang L and Zhu J 2017 Study of network topology effect on measurement accuracy for a distributed rotary-laser measurement system *Opt. Eng.* **56** 094101

[33] Zhang R, Shi S and Lin J Yang S and Yang L 2022 Calibration and measurement space inconsistency analysis for workshop measurement positioning system (wMPS) *Proc. SPIE* **12282** 171–7

[34] Zhao Z, Zhu J, Xue B and Yang L 2014 Optimization for calibration of large-scale optical measurement positioning system by using spherical constraint *J. Opt. Soc. Am.* A **31** 1427–35